The Journal of Physical Chemistry Letters

Surfaces, Interfaces, and Catalysis; Physical Properties of Nanomaterials and Materials

Defects in Highly Anisotropic Transition-Metal Dichalcogenide PdSe

Mingming Fu, Liangbo Liang, Qiang Zou, Giang D Nguyen, Kai Xiao, An-Ping Li, Junyong Kang, Zhiming Wu, and Zheng Gai

J. Phys. Chem. Lett., **Just Accepted Manuscript** • DOI: 10.1021/acs.jpclett.9b03312 • Publication Date (Web): 27 Dec 2019

Defects in Highly Anisotropic Transition-Metal Dichalcogenide $PdSe_2$

Mingming Fu[1,2], Liangbo Liang[2], Qiang Zou[2], Giang D. Nguyen[2], Kai Xiao[2], An-Ping Li[2], Junyong Kang[1], Zhiming Wu[1,*], and Zheng Gai[2,*]

[1]Fujian Provincial Key Laboratory of Semiconductors and Applications, Collaborative Innovation Center for Optoelectronic Semiconductors and Efficient Devices, Department of Physics, Xiamen University, Xiamen, Fujian Province, 361005, P. R. China

[2]Center for Nanophase Materials Sciences, Oak Ridge National Laboratory, Oak Ridge, TN 37831, USA

[*] Corresponding author: gaiz@ornl.gov, zmwu@xmu.edu.cn

Abstract

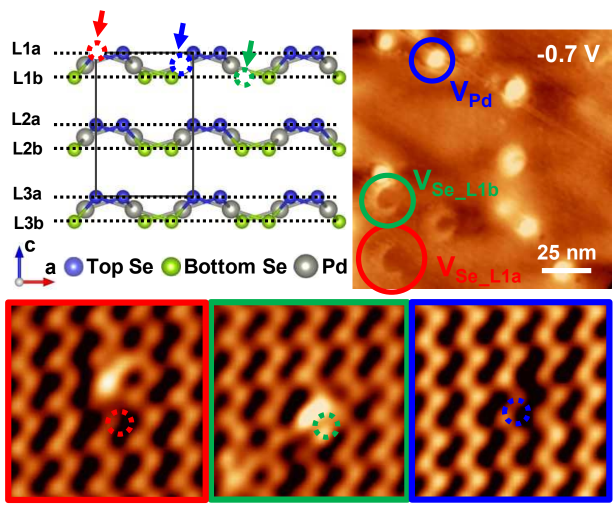

The atomic and electronic structures of the pristine $PdSe_2$ as well as various intrinsic vacancy defects in $PdSe_2$ are studied comprehensively by combining scanning tunneling microscopy, spectroscopy and density functional theory calculations. Other than the topmost Se atoms, sublayer Pd atoms, the intrinsic Pd and Se vacancy-defects are identified. Both V_{Se} and V_{Pd} defects induce defect states near Fermi level. As a result, the vacancy defects can be negatively charged by tip gating effect. At negative sample bias, the screened Coulomb interaction between STM tip and the charged vacancies creates disk-like protrusion around V_{Pd} and crater-like features around V_{Se}. The magnification effect of the long-range charge localization at the charged defect site makes sublayer defects as deep as 1nm visible even in STM images. This result proves that by gating the probe, scanning probe microscopy can be used as an easy tool for characterizing sublayer defects in a nondestructive way.

Keywords: 2D material, Scanning Probe Microscopy, $PdSe_2$, point defect.

Two dimensional (2D) materials have been studied extensively, due to the unique and unusual properties that promise novel applications[1-7]. The application of atomically thick 2D materials in devices makes their optical and electronic properties particularly sensitive to local stimulus like defects or edge states in graphene and transition metal dichalcogenide (TMDs)[8-12]. The defects in TMDs can significantly alter their physical and chemical properties[13]. As an example, in MoS_2, the most promising electro-catalytic processes candidate, sulfur vacancies are newly discovered to be active sites for electrochemical hydrogen evolution[14-16]. The intrinsic activity can be optimized by fine tuning the S-vacancy concentration and introducing elastic tensile strain, but the role of these S-vacancy sites in the hydrogen evolution reaction catalysts are still unknown. Therefore, *in-situ* and nondestructive characterization of vacancy defects, which are not only on surface, most importantly few layers underneath the surface, is crucial in the tuning process.

Among the family of semiconducting TMDs, $PdSe_2$ with an uncommon pentagonal structure has recently attracted a lot of attention as a potential material for 2D electronic devices because of its high carrier mobility[17], thickness-dependent band gaps[18-20], air stability and high photoresponsivity[21]. The monolayer $PdSe_2$ pentagonal structure is formed by a tilted Se-Se dumbbell crossing the Pd layer, which results in the lack of rotational symmetry[18, 22]. Such a structure is potentially sensitive to defects, as Se vacancies would break the symmetry of the Se-Se dumbbell and induce large structural distortion[22]. Therefore, understanding the defect behavior in $PdSe_2$ is important for its practical device application. We have reported previously that by taking advantage of tip-induced band bending (TIBB) effect[23-25], conductance map can be utilized to image Se vacancy (V_{Se}) in a 3D manner, and scanning tunneling microscopy (STM) tip can be used to manipulate the V_{Se}[26].

In this paper, we extensively study the atomic and electronic structures of pristine $PdSe_2$ and various intrinsic vacancy defects in $PdSe_2$. Although the Pd atoms are not on the topmost surface as Se atoms are, special STM imaging conditions are found to visualize them. The bias-dependent STM images of pristine $PdSe_2$ are corroborated by simulated ones using first-principles density functional theory (DFT) calculations. Compared to the topmost surface Se atoms that are visible all the time, the underneath Pd atoms can be imaged at energy lower than -1 eV where the contribution of the Pd's 4d orbitals to the total DOS grows stronger. Besides the pristine surface, the intrinsic Pd and Se vacancy-defects can also be identified by combining STM image, STS spectra and DFT calculations. Consistent with calculations, both V_{Se} and V_{Pd} defects induce a defect state near the Fermi energy. The vacancy defects can be negatively charged by tip gating effect. At negative sample bias, the screened Coulomb interaction between STM tip and the charged vacancies creates disk-like protrusion around V_{Pd} and crater-like features around V_{Se}. The magnification effect of the long-range charge localization at the charged defect site renders sublayer defects as deep as 1nm visible even in STM images. This result provides STM imaging itself as an easy tool for characterizing sublayer defects in a nondestructive way. We anticipate that the same method can be used widely for other 2D materials and other probing tools, for example, by gating with the probe of atomic force microscopy.

The $PdSe_2$ single crystals were synthesized by a self-flux method as reported[18]. The crystal was cleaved *in situ* at low temperature in an ultra-high vacuum. All the experiments were performed using an Unisoku low-temperature STM with chemically etched tungsten tips at a cryogenic temperature of 77 K under a base pressure of 1×10^{-10} Torr. Calculations were carried out using the plane-wave DFT software VASP[27-28]. Electronic exchange-correlation interaction was described with the generalized gradient approximation (GGA) and the Perdew-Burke-Ernzerhof (PBE) functional in combination with projector augmented wave (PAW) pseudopotentials[29]. Van der Waals (vdW) interactions between the $PdSe_2$ layers were considered using the vdW density functional method optPBE-vdW[30]. For bulk $PdSe_2$, both atomic coordinates and lattice constants were optimized until the atom force convergence was below 0.01 eV/Å, with a cutoff energy at 350 eV and a 12×12×8 k-point sampling. Then six-layer $PdSe_2$ structure was built to simulate the surface by a periodic slab geometry with a vacuum separation of 21 Å in the out-of-plane direction and a 12×12×1 k-point sampling. All atoms were relaxed until the residual forces below 0.01 eV/Å and in-plane lattice constants were also optimized. To simulate defects on the surface, a 4×4×1 supercell structure of the six-layer $PdSe_2$ surface was considered, where various types of vacancy, such as a single Se or Pd vacancy, were introduced. For the supercell structure the atoms were relaxed until the residual forces were below 0.02 eV/Å, where a reduced k-point sampling (3×3×1) was used. STM images were simulated using converged electronic densities within the Tersoff-Hamann approximation.

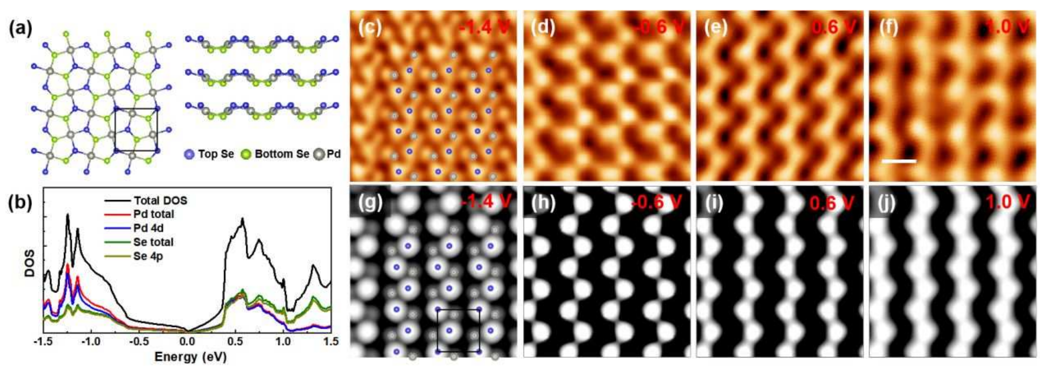

Fig. 1. Bias dependent STM images of pristine $PdSe_2$ surface. (a) Top view and side view of the lattice structure of $PdSe_2$ with the blue, green and gray spheres representing the top Se, bottom Se and Pd atoms, respectively. (b) Calculated density of states of bulk $PdSe_2$. The Fermi energy is set to zero. (c-f) Atomically resolved STM images at bias -1.4 V, -0.6 V, 0.6V and 1.0 V. The scale bar is 0.5 nm. (g-j) Simulated STM images of $PdSe_2$ at corresponding biases.

The $PdSe_2$ surface has a strong bias dependent behavior as most of the semiconductors do. The crystal is cleaved in-between the Se-Pd-Se trilayer slabs, with the topmost Se atoms in two equivalent sites as shown in Fig. 1(a). Pd atoms are 0.074 nm underneath the top Se layer. Figs. 1(c)-(f) show atomically resolved STM images of $PdSe_2$ at different bias voltage. While at most of biases, only those Se atoms in the zigzag chains from the topmost Se layer are visible in the STM images, the signal of Pd atoms underneath can be detected at relatively large negative bias (valance band), as shown in Fig. 1(c) at -1.4 V, which are in agreement with the simulated STM images shown in Figs. 1(g)-(j). The origin of the Pd contrast comes from the stronger contribution of the 4d electron band of the Pd atoms to the total DOS at energy lower than -1 eV, as shown in the calculated total and partial DOS plot in Fig. 1(b) and a previous theoretical work [31]. Since the Pd 4d state (blue line in Fig. 1(b)) is suppressed as the bias getting closer to the Fermi level and in the conduction band, the STM images start to reflect the surface morphology more, so only the zigzag chains composed of the Se atoms on the topmost layer appear as shown in Figs. 1 (d)-(f) and their simulated images in Figs. 1(h)-(j).

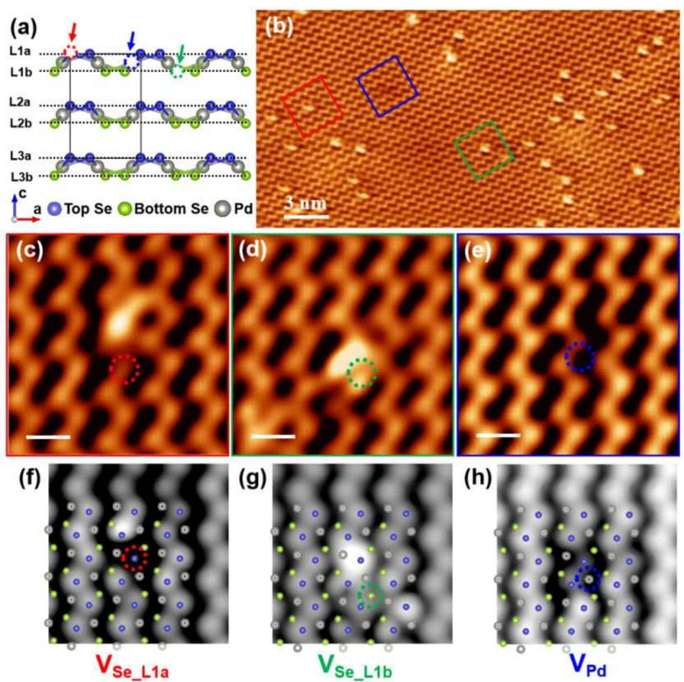

Fig. 2. STM images of defects on $PdSe_2$. (a) Side view of the lattice structure of $PdSe_2$. L1a; L1b; ..., define Se sublayers along the c direction where the Se top surface layer is counted as layer L1a[26]. The black rectangle outlines the unit cell. (b) A typical STM topographic image of $PdSe_2$ surface, where three types of defects are outlined (V_s = 0.6 V, I = 50 pA). (c)-(e) Zoomed in images of the red, green and blue

square areas in (b), revealing the L1a Se vacancy (V_{Se_L1a}), L1b Se vacancy (V_{Se_L1b}) and Pd vacancy (V_{Pd}) (see text) marked by dashed circles respectively. The scale bar is 0.56 nm. (f-h) Simulated STM images of three types of defects, respectively, with the $PdSe_2$ lattice structure overlaid on top, and dashed circles highlighting the defect locations.

The natural cleavage surface of $PdSe_2$ is never defect free. Actually, many interesting physical properties are originated from the existence of various defects in the crystal. Fig. 2(b) is a typical large area STM image from the $PdSe_2$ surface in atomic resolution showing randomly distributed defects. With the help of atomically resolved bias dependent images and spectroscopy images, these defects can be classified into three types as marked in red, green and blue squares. The zoom-in images of the red, green and blue squares are shown in Figs. 2(c)-2(e), respectively. The first type of defect shown in Fig. 2(c) is represented by a dark region marked by the red circle and a bright protrusion on the top Se position. The second type of defect is shown in Fig. 2(d), apparently with only bright protrusion regions near the defect area. The darkest region in the third type defect is in-between the Se zigzag chain and extend to the neighboring Se atoms, as shown in Fig. 2(e). The third type is less common than the other two types. To identify the origin of the defects, DFT calculations of various defect configurations, including Se and Pd single vacancy as well as Pd and oxygen substitutional doping, are performed. The simulated STM images with missing Se atom (top or bottom Se sublayer) and missing Pd atom, as circled in red, green and blue in Fig. 2(a), resemble the experimental data well. Fig. 2(f) shows a simulated STM image of a single Se vacancy on the topmost layer (V_{Se_L1a}). The missing of a L1a Se atom has asymmetric influence on the two neighboring Se atoms, which matches well with the experimental image in Fig. 2(c). This behavior is due to the inequivalent neighboring Se atoms in the unique pentagonal lattice structure of $PdSe_2$. The removal of the L1a Se atom relaxes only Pd atom on one side but both Pd and bottom Se on the other side. As a result, there is almost no contrast change on one side, but on the other side, a bright protrusion is created due to the upward relaxation of the Se atom and the pop up of the Pd atom. The L1b Se vacancy (i.e., missing bottom layer Se atom) introduces dangling bonds and causes reconfiguration of nearby atoms, and it creates a bright protrusion rather than a dark area as shown in the simulated and experimental images in Figs. 2(g) and (d), respectively. The asymmetric pentagonal lattice again plays a role in the resulted images. In Fig. 2(h), we show a simulated STM image of a single V_{Pd} defect located on the topmost PdSe2 layer. Our calculations found that the missing Pd atom leads to downward relaxation of the two Se atoms bonded with it, and therefore the two Se atoms are apparently darker than others, which is consistent with the STM image in Fig. 2(e).

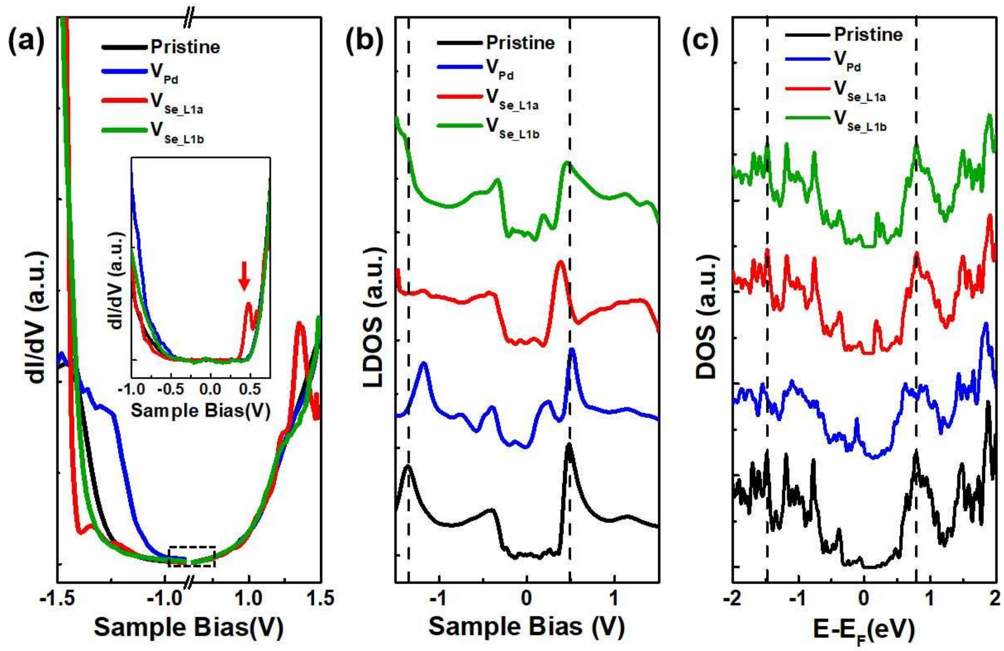

Fig. 3. Experimental dI/dV spectra (a) and LDOS ((dI/dV)/(I/V)) spectra (b) taken at the V_{Pd}, V_{Se_L1a}, and V_{Se_L1b} of the topmost $PdSe_2$ layer and pristine $PdSe_2$. Inset in (a) shows the zoomed in dI/dV curves from -1.0 V to 0.75 V. For comparison, DFT calculated DOS corresponding to V_{Pd}, V_{Se_L1a} and V_{Se_L1b} as well as the pristine $PdSe_2$

is also shown in (c).

The comparison of the dI/dV spectra and LDOS of three types of defects and the pristine $PdSe_2$ is shown in Fig. 3(a) and 3(b), respectively. At higher bias voltage in both conduction and valance band, the existence of the Se vacancy creates sharp peaks compared to the pristine dI/dV spectra. In the low energy conduction band, a clear peak is observed at the dI/dV spectrum of V_{Se_L1a} as shown by an arrow in the inset of Fig. 3(a). As discussed in detail later in this paper, this state is very localized, and it is a new peak created by Se vacancy rather than a shift of the pristine-state at 0.5 V in the LDOS. The V_{Se_L1b} defect spectrum is similar but less pronounced than the V_{Se_L1a} defect spectrum. The main feature of the V_{Pd} spectrum is the peak at -1.2 V and a new state near the Fermi level (+0.2 V) as shown in Fig. 3(b). The calculated DOS curves for the pristine surface and three vacancy defects are shown in Fig. 3(c), which reveal that the Se and Pd vacancies induce localized defect states near the Fermi level, consistent with the experimental trends. Note that the energy levels of the defect states in the calculations cannot be quantitatively compared with experimental data for two reasons: one arises from the limitation of the DFT theory such as the approximation for the exchange-correlation functional; the other is related to the limited supercell size and number of layers involved in the calculations due to computational cost (see the Method).

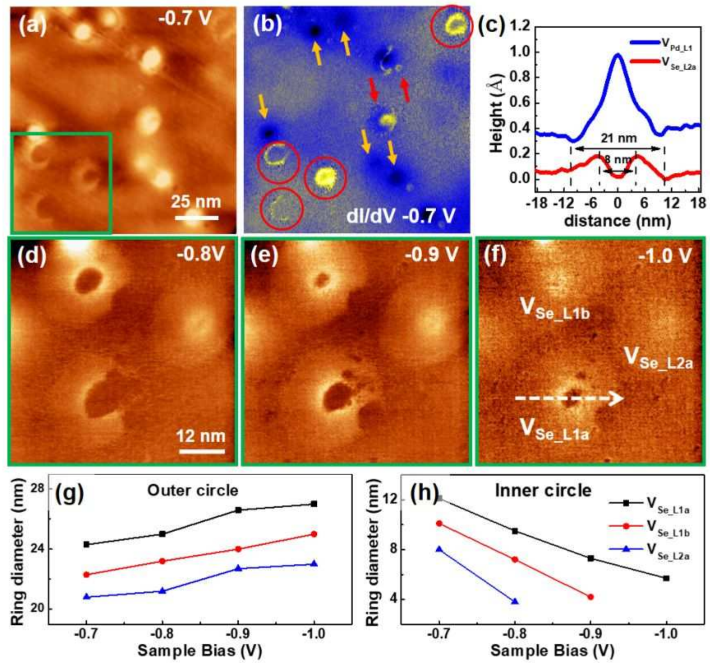

Fig. 4 (a)-(b) STM topographic image and corresponding dI/dV map at a sample bias voltage of -0.7 V. Red circles, red and yellow arrows mark vacancy defects (see text). (c) Line profiles taken across a V_{Pd} (blue) and a V_{Se} (red), respectively. (d)-(f) Sample bias dependence of STM topographic images of three V_{Se} located at different lattice layers (labeled in (f)), same as the green square area of (a). (g) and (h) The change of outer and inner circle diameter as a function of sample bias.

We demonstrated previously that the V_{Se} defects (surface and subsurface) can be imaged as circular-ring features in spatially resolved differential conductance dI/dV maps under positive sample bias range from 0.9 V, as a result of defect charge state from V^0 to V^- due to TIBB effect [26]. However, for negative sample bias, which means at a condition of pushing further for the negatively charged states, the STM image and spectroscopy become quite complicated. Fig. 4 (a) and (b) show a pair of typical negative sample bias topographic image form $PdSe_2$ surface and corresponding dI/dV map collected simultaneously. By combining the two images, three types of features are observed, labeled by red circles, yellow and red arrows. By comparing the positive and negative bias images as well as atomically resolved images and spectra described above, we identify that the features with red circles and yellow arrows are V_{Se} defects and V_{Pd} defects, respectively. The red arrows point to close-packed defect combos of V_{Se} + V_{Pd}. The line profiles in Fig. 4(c) show the qualitatively different topographic features of V_{Se} and V_{Pd} defects from the -0.7 V STM image. While the V_{Pd} shows a disk-like protrusion, V_{Se} defect has a crater-like feature, with an 21 nm outer-circle of the enhancement disk and a depression region started at an 8 nm inner-circle. The inner-circles are also imaged as bright rings in the differential dI/dV maps (Fig. 4(b)).

The size and contrast of the crater (V_{Se}) and disk (V_{Pd}) in STM images depend on the depth of the defects from the surface, and of course also depend on the sample bias of imaging. The Pd vacancies at the L3 and L4 layers (Fig. 4(a) and (b)) can be easily recognized from even the STM image, which is more than 1 nm underneath the surface. The bias dependent images from the three V_{Se} defects (V_{Se_L1a}, V_{Se_L1b} and V_{Se_L2a} as labeled in Fig. 4(f)) in the green square area in Fig. 4(a) are shown in Figs. 4(d)-4(f). The sample bias dependence of the inner and outer circles for the three defects at different subsurface layers is shown in Fig. 4(g) and (h). While the size of the outer-circle increases slightly when the sample bias changes from -0.7 V to -1.0 V, the size of the inner-circle decreases. A similar crater-like feature was previously observed in single-atom dangling bond defect with a bound state below the conduction band in silicon, an sp^3 orbital facing a silicon atom vacancy[32].

The outer-circle is the long-range effects of charge localization at the defect site. The sample bias dependence is the result of the screened Coulomb potentials with the STM tip playing a role as a gate. The electrostatic gating effect of the tip on the substrate scales with bias, so as the size of the outer-circle[33]. The similar enhanced ionization range around charged defects (vacancies or substitutes) has also been described in GaAs[23], graphene[34] and Al_2O_3/NiAl[35]. As for the reason of weaker bias dependence for V_{Se_L1b} and V_{Se_L2a} than V_{Se_L1a} (Fig. 4(g)), as demonstrated in the numerical simulation previously[33] that the electrostatic potential created by tip is drastically different underneath (0.15 nm for V_{Se_L1b} and 0.43 nm for V_{Se_L2a}) or on the surface (V_{Se_L1a}) of samples.

The inner-circle of the crater feature is a result of non-equilibrium charging effect. As the tip moves closer to the vacancy defect, a depression region (~8 nm across in Fig. 4 (c)) that surrounds the Se vacancy indicates that the defect does not remain negatively charged. This is analogues to a single electron transistor (SET) case as analyzed in detail for dangling bond defect at silicon surface[32]. The STM tip is similar to the gate in a SET. The negative sample bias results in an electron accumulation region around the V_{Se}, which decouples the vacancy from the $PdSe_2$ bulk. Then the charging strength of the V_{Se} is then governed by the electron transfer rates on and off the defect, rather than by the band bending effect. As a consequence of the lower tunneling rate between the tip and sample, which is proportional to the transmission probability and tip LDOS, the spatial extent of the inner-circle decreases with increasing sample bias value (from -0.7V to -1.0V) as shown in Fig. 4 (h).

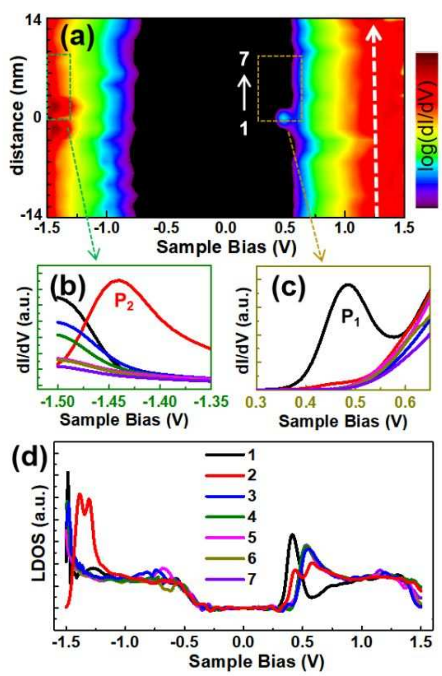

Fig. 5. (a) Color map of a log(dI/dV) taken crossing a V_{Se_L1a} along the white dashed arrow in Fig. 4(f). 7 characteristic dI/dV and LDOS curves are shown in

(b)-(d). (b)-(c) Spatially resolved dI/dV spectra corresponding to the green dashed square and yellow dashed square in (a), respectively.

The dI/dV map of the V_{Se} further reveals the nature of the crater feature. Shown in Fig. 5 are line spectra collected crossing one of the V_{Se_L1a}. Fig. 5(a) is a 3D color map of log(dI/dV) line profile as a function of sample bias and position taken across a V_{Se_L1a} defect (positioned at 0 nm) marked with white arrow in Fig. 4(f). The bright spot in the conduction band (around 0.5 V) is observed right at the Se defect position corresponds to the peak P_1 in the black "1" spectrum in Fig. 5(c), which is the defect state near the band edge as described above. In the corresponding LDOS spectra in Fig. 5(d), the intensity of the defect state gradually decreases while the intensity of the 0.5 V pristine-state increases from "1" to "2" and "3" spectra. In other words, the influence range of the Se vacancy defect state to the conduction band is less than 3 nm (5 unit cells). On the valance band side, as shown in Fig. 5(a), there are two areas at the bias voltage around -1.4 V located on both sides of the V_{Se_L1a} defect, with a distance of 5 nm (close to the inner-circle edge), which corresponds to the peak P_2 in red "2" spectrum [Fig. 5(b)], same as the valance band state of pristine $PdSe_2$ as shown in Fig. 3(b). When crossing over the inner-circle edge, the -1.4 V valance band state is bending toward the higher energy direction as discussed above, shown as curves 2-7 in Fig. 5(b).

Pd vacancies also show similar depth dependence. As shown in Fig. 6, Pd vacancies which locate at the L1, L2 and L3 Pd sublayers show different height protrusions in STM topographic images and different depth holes in dI/dV maps. As the Pd vacancies locate deeper, the height of protrusions in STM images and the depth of holes in dI/dV maps become weaken.

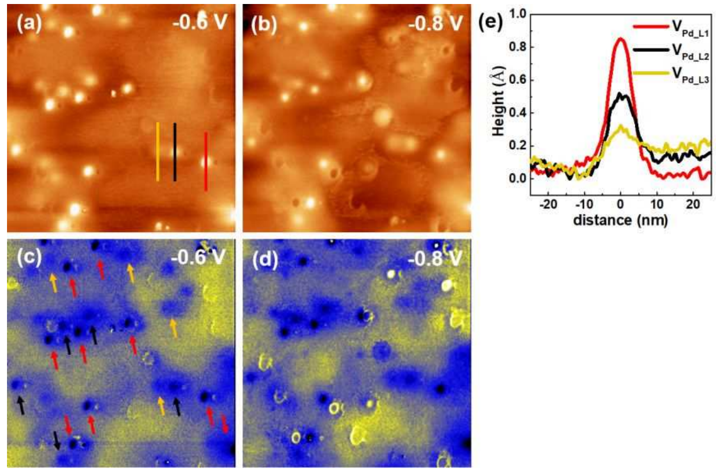

Fig. 6 (a)-(b) and (c)-(d) STM topographic images and corresponding dI/dV maps at the sample bias voltage of -0.6 V and -0.8V, respectively. The red, black, and yellow arrows represent Pd vacancies located at the L1, L2 and L3 Pd sublayers, respectively. (e) Line profiles taken along the red, black, and yellow lines in (a), respectively.

In summary, we found the bias-dependent STM images of pristine $PdSe_2$, which are corroborated by DFT calculations. Although the topmost surface Se atoms are visible all the time, the underneath Pd atoms can only be imaged at energy lower than -1 eV where the contribution of the 4d electron bands of the Pd atoms to the total DOS grows stronger. Furthermore, the intrinsic Pd and Se vacancy defects can be identified by combining STM images, STS spectra and DFT calculations. Both V_{Se} and V_{Pd} defects induce a defect state near the Fermi energy. The vacancy defects can be negatively charged by tip gating effect. As a result, at negative sample bias, the screened Coulomb interaction between STM tip and the charged vacancies creates disk-like protrusion around V_{Pd} and crater-like features around V_{Se}. The long-range of charge localization at the defect site magnifies the influence of the vacancy defects, rendering sublayer defects as deep as 1nm visible even in STM images. Similar defects are widely exist in MoS_2 and other 2D systems[36-39], and this work demonstrates STM imaging as a powerful tool for ready characterization of surface and subsurface defects for applications of 2D materials[16, 19, 21]. We believe that by gating the cantilever of atomic force microscopy, the same method can be extended to other imaging technique in SPM family for defect characterizations.

Acknowledgements

This research was conducted at the Center for Nanophase Materials Sciences, which is a DOE Office of Science User Facility. M.F. was supported by the China Scholarship Council.

Data Availability

The data sets that support the findings in this study are available from the corresponding author upon reasonable request.

Author contributions

M.F, Q.Z., and Z.G. conducted the STM/S studies and data analysis; L. L. conducted DFT calculations; all authors contributed to the discussion and writing of the manuscript.

Competing interests

The authors declare no competing interests.

References

1. Geim, A. K.; Grigorieva, I. V. Van der Waals heterostructures. *Nature* **2013,** *499* (7459), 419-425.

2. Novoselov, K. S.; Geim, A. K.; Morozov, S. V.; Jiang, D.; Zhang, Y.; Dubonos, S. V.; Grigorieva, I. V.; Firsov, A. A. Electric field effect in atomically thin carbon films. *Science* **2004,** *306* (5696), 666-669.

3. Cho, S.; Kim, S.; Kim, J. H.; Zhao, J.; Seok, J.; Keum, D. H.; Baik, J.; Choe, D. H.; Chang, K. J.; Suenaga, K.; Kim, S. W.; Lee, Y. H.; Yang, H. Phase patterning for ohmic homojunction contact in MoTe2. *Science* **2015,** *349* (6248), 625-628.

4. Xi, X. X.; Zhao, L.; Wang, Z. F.; Berger, H.; Forro, L.; Shan, J.; Mak, K. F. Strongly enhanced charge-density-wave order in monolayer NbSe2. *Nat Nanotechnol* **2015,** *10* (9), 765.

5. Zhao, Y. D.; Qiao, J. S.; Yu, P.; Hu, Z. X.; Lin, Z. Y.; Lau, S. P.; Liu, Z.; Ji, W.; Chai, Y. Extraordinarily Strong Interlayer Interaction in 2D Layered PtS2. *Adv Mater* **2016,** *28* (12), 2399-2407.

6. Zheng, H. S.; Choi, Y.; Baniasadi, F.; Hu, D. K.; Jiao, L. Y.; Park, K.; Tao, C. G. Visualization of point defects in ultrathin layered 1T-PtSe2. *2d Mater* **2019,** *6* (4), 041005.

7. Barja, S.; Refaely-Abramson, S.; Schuler, B.; Qiu, D. Y.; Pulkin, A.; Wickenburg, S.; Ryu, H.; Ugeda, M. M.; Kastl, C.; Chen, C.; Hwang, C.; Schwartzberg, A.; Aloni, S.; Mo, S. K.; Ogletree, D. F.; Crommie, M. F.; Yazyev, O. V.; Louie, S. G.; Neaton, J. B.; Weber-Bargioni, A. Identifying substitutional oxygen as a prolific point defect in monolayer transition metal dichalcogenides. *Nat Commun* **2019,** *10*, 3382.

8. Liu, H. J.; Zheng, H.; Yang, F.; Jiao, L.; Chen, J. L.; Ho, W. K.; Gao, C. L.; Jia, J. F.; Xie, M. H. Line and Point Defects in MoSe2 Bilayer Studied by Scanning Tunneling Microscopy and Spectroscopy. *Acs Nano* **2015,** *9* (6), 6619-6625.

9. Le, D.; Rawal, T. B.; Rahman, T. S. Single-Layer MoS2 with Sulfur Vacancies: Structure and Catalytic Application. *J Phys Chem C* **2014,** *118* (10), 5346-5351.

10. Hus, S. M.; Li, A. P. Spatially-resolved studies on the role of defects and boundaries in electronic behavior of 2D materials. *Prog Surf Sci* **2017,** *92* (3), 176-201.

11. Zhang, S.; Wang, C. G.; Li, M. Y.; Huang, D.; Li, L. J.; Ji, W.; Wu, S. W. Defect Structure of Localized Excitons in a WSe2 Monolayer. *Phys Rev Lett* **2017,** *119* (4), 046101.

12. Zhou, W.; Zou, X. L.; Najmaei, S.; Liu, Z.; Shi, Y. M.; Kong, J.; Lou, J.; Ajayan, P. M.; Yakobson, B. I.; Idrobo, J. C. Intrinsic Structural Defects in Monolayer Molybdenum Disulfide. *Nano Lett* **2013,** *13* (6), 2615-2622.

13. Lin, Z.; Carvalho, B. R.; Kahn, E.; Lv, R. T.; Rao, R.; Terrones, H.; Pimenta, M. A.; Terrones, M. Defect engineering of two-dimensional transition metal dichalcogenides. *2d Mater* **2016,** *3* (2), 022002.

14. Hinnemann, B.; Moses, P. G.; Bonde, J.; Jorgensen, K. P.; Nielsen, J. H.; Horch, S.; Chorkendorff, I.; Norskov, J. K. Biornimetic hydrogen evolution: MoS2 nanoparticles as catalyst for hydrogen evolution. *J Am Chem Soc* **2005,** *127* (15), 5308-5309.

15. Jaramillo, T. F.; Jorgensen, K. P.; Bonde, J.; Nielsen, J. H.; Horch, S.; Chorkendorff, I. Identification of active edge sites for electrochemical H-2 evolution from MoS2 nanocatalysts. *Science* **2007,** *317* (5834), 100-102.

16. Li, H.; Tsai, C.; Koh, A. L.; Cai, L. L.; Contryman, A. W.; Fragapane, A. H.; Zhao, J. H.; Han, H. S.; Manoharan, H. C.; Abild-Pedersen, F.; Norskov, J. K.; Zheng, X. L. Activating and optimizing MoS2 basal planes for hydrogen evolution through the formation of strained sulphur vacancies. *Nat Mater* **2016,** *15* (1), 48-53.

17. Chow, W. L.; Yu, P.; Liu, F. C.; Hong, J. H.; Wang, X. L.; Zeng, Q. S.; Hsu, C. H.; Zhu, C.; Zhou, J. D.;

Wang, X. W.; Xia, J.; Yan, J. X.; Chen, Y.; Wu, D.; Yu, T.; Shen, Z. X.; Lin, H.; Jin, C. H.; Tay, B. K.; Liu, Z. High Mobility 2D Palladium Diselenide Field-Effect Transistors with Tunable Ambipolar Characteristics. *Adv Mater* **2017,** *29* (21), 1602969.

18. Oyedele, A. D.; Yang, S. Z.; Liang, L. B.; Puretzky, A. A.; Wang, K.; Zheng, J. J.; Yu, P.; Pudasaini, P. R.; Ghosh, A. W.; Liu, Z.; Rouleau, C. M.; Sumpter, B. G.; Chisholm, M. F.; Zhou, W.; Rack, P. D.; Geohegan, D. B.; Xiao, K. PdSe2: Pentagonal Two-Dimensional Layers with High Air Stability for Electronics. *J Am Chem Soc* **2017,** *139* (40), 14090-14097.

19. Zeng, L. H.; Chen, Q. M.; Zhang, Z. X.; Wu, D.; Yuan, H.; Li, Y. Y.; Qarony, W.; Lau, S. P.; Luo, L. B.; Tsang, Y. H. Multilayered PdSe2/Perovskite Schottky Junction for Fast, Self-Powered, Polarization-Sensitive, Broadband Photodetectors, and Image Sensor Application. *Adv Sci (Weinh)* **2019,** *6* (19), 1901134.

20. Puretzky, A. A.; Oyedele, A. D.; Xiao, K.; Haglund, A. V.; Sumpter, B. G.; Mandrus, D.; Geohegan, D. B.; Liang, L. B. Anomalous interlayer vibrations in strongly coupled layered PdSe2. *2d Mater* **2018,** *5* (3), 035016.

21. Liang, Q.; Wang, Q.; Zhang, Q.; Wei, J.; Lim, S. X.; Zhu, R.; Hu, J.; Wei, W.; Lee, C.; Sow, C.; Zhang, W.; Wee, A. T. S. High-Performance, Room Temperature, Ultra-Broadband Photodetectors Based on Air-Stable PdSe2. *Adv Mater* **2019,** *31* (24), e1807609.

22. Lin, J. H.; Zuluaga, S.; Yu, P.; Liu, Z.; Pantelides, T.; Suenaga, K. Novel Pd2Se3 Two-Dimensional Phase Driven by Interlayer Fusion in Layered PdSe2. *Phys Rev Lett* **2017,** *119* (1), 016101.

23. Teichmann, K.; Wenderoth, M.; Loth, S.; Ulbrich, R. G.; Garleff, J. K.; Wijnheijmer, A. P.; Koenraad, P. M. Controlled charge switching on a single donor with a scanning tunneling microscope. *Phys Rev Lett* **2008,** *101* (7), 076103.

24. Marczinowski, F.; Wiebe, J.; Tang, J. M.; Flatte, M. E.; Meier, F.; Morgenstern, M.; Wiesendanger, R. Local electronic structure near mn acceptors in InAs: Surface-induced symmetry breaking and coupling to host states. *Phys Rev Lett* **2007,** *99* (15), 157202.

25. Song, C. L.; Jiang, Y. P.; Wang, Y. L.; Li, Z.; Wang, L. L.; He, K.; Chen, X.; Ma, X. C.; Xue, Q. K. Gating the charge state of single Fe dopants in the topological insulator Bi2Se3 with a scanning tunneling microscope. *Phys Rev B* **2012,** *86* (4), 045441.

26. Nguyen, G. D.; Liang, L. B.; Zou, Q.; Fu, M. M.; Oyedele, A. D.; Sumpter, B. G.; Liu, Z.; Gai, Z.; Xiao, K.; Li, A. P. 3D Imaging and Manipulation of Subsurface Selenium Vacancies in PdSe2. *Phys Rev Lett* **2018,** *121* (8), 086101.

27. Kresse, G.; Furthmuller, J. Efficiency of ab-initio total energy calculations for metals and semiconductors using a plane-wave basis set. *Comp Mater Sci* **1996,** *6* (1), 15-50.

28. Kresse, G.; Furthmuller, J. Efficient iterative schemes for ab initio total-energy calculations using a plane-wave basis set. *Phys Rev B* **1996,** *54* (16), 11169-11186.

29. Perdew, J. P.; Burke, K.; Ernzerhof, M. Generalized gradient approximation made simple. *Phys Rev Lett* **1996,** *77* (18), 3865-3868.

30. Dion, M.; Rydberg, H.; Schroder, E.; Langreth, D. C.; Lundqvist, B. I. Van der Waals density functional for general geometries. *Phys Rev Lett* **2004,** *92* (24), 246401.

31. Sun, J. F.; Shi, H. L.; Siegrist, T.; Singh, D. J. Electronic, transport, and optical properties of bulk and mono-layer PdSe2. *Appl Phys Lett* **2015,** *107* (15), 153902.

32. Schofield, S. R.; Studer, P.; Hirjibehedin, C. F.; Curson, N. J.; Aeppli, G.; Bowler, D. R. Quantum engineering at the silicon surface using dangling bonds. *Nat Commun* **2013,** *4*, 1649.

33. Feenstra, R. M. Electrostatic potential for a hyperbolic probe tip near a semiconductor. *J Vac Sci Technol B* **2003,** *21* (5), 2080-2088.

34. Zhang, Y. B.; Brar, V. W.; Girit, C.; Zettl, A.; Crommie, M. F. Origin of spatial charge inhomogeneity in graphene (vol 5, pg 722, 2009). *Nat Phys* **2010,** *6* (1), 74-74.

35. Pradhan, N. A.; Liu, N.; Silien, C.; Ho, W. Atomic scale conductance induced by single impurity charging. *Phys Rev Lett* **2005,** *94* (7), 076801.

36. Liu, M. X.; Shi, J. P.; Li, Y. C.; Zhou, X. B.; Ma, D. L.; Qi, Y.; Zhang, Y. F.; Liu, Z. F. Temperature-Triggered Sulfur Vacancy Evolution in Monolayer MoS2/Graphene Heterostructures. *Small* **2017,** *13* (40), 1602967.

37. Addou, R.; Colombo, L.; Wallace, R. M. Surface Defects on Natural MoS2. *Acs Appl Mater Inter* **2015,** *7* (22), 11921-11929.

38. Guguchia, Z.; Kerelsky, A.; Edelberg, D.; Banerjee, S.; von Rohr, F.; Scullion, D.; Augustin, M.; Scully, M.; Rhodes, D. A.; Shermadini, Z.; Luetkens, H.; Shengelaya, A.; Baines, C.; Morenzoni, E.; Amato, A.; Hone, J. C.; Khasanov, R.; Billinge, S. J. L.; Santos, E.; Pasupathy, A. N.; Uemura, Y. J. Magnetism in semiconducting molybdenum dichalcogenides. *Sci Adv* **2018,** *4* (12), eaat3672.

39. Das, P. K.; Di Sante, D.; Vobornik, I.; Fujii, J.; Okuda, T.; Bruyer, E.; Gyenis, A.; Feldman, B. E.; Tao, J.; Ciancio, R.; Rossi, G.; Ali, M. N.; Picozzi, S.; Yazdani, A.; Panaccione, G.; Cava, R. J. Layer-dependent quantum cooperation of electron and hole states in the anomalous semimetal WTe2. *Nat Commun* **2016,** *7*, 10847.

This manuscript has been authored by UT-Battelle, LLC under Contract No. DE-AC05-00OR22725 with the U.S. Department of Energy. The United States Government retains and the publisher, by accepting the article for publication, acknowledges that the United States Government retains a non-exclusive, paid-up, irrevocable, world-wide license to publish or reproduce the published form of this manuscript, or allow others to do so, for United States Government purposes. The Department of Energy will provide public access to these results of federally sponsored research in accordance with the DOE Public Access Plan (http://energy.gov/downloads/doe-public-access-plan)